PAPER

Electronic and optical properties of boron-based hybrid monolayers

View the article online for updates and enhancements.

Electronic and optical properties of boron-based hybrid monolayers

Neha Katoch[1,*] , **Ashok Kumar**[2] , **Jagdish Kumar**[1,*] , **P K Ahluwalia**[3] **and Ravindra Pandey**[4]

[1] Department of Physics and Astronomical Science, School of Physical and Material Sciences, Central University of Himachal Pradesh, Dharamshala, 176206, India
[2] Department of Physics, School of Basic Sciences, Central University of Punjab, Bathinda, 151401, India
[3] Department of Physics, Himachal Pradesh University, Shimla, 171005, India
[4] Department of Physics, Michigan Technological University, Houghton, MI 49931, United States of America

E-mail: nehakatoch2@gmail.com and jagdishphysicist@gmail.com

Abstract

Anisotropic 2D Dirac cone materials are important for the fabrication of nanodevices having direction-dependent characteristics since the anisotropic Dirac cones lead to different values of Fermi velocities yielding variable carrier concentrations. In this work, the feasibility of the B-based hybrid monolayers BX (X = As, Sb, and Bi), as anisotropic Dirac cone materials is investigated. Calculations based on density functional theory and molecular dynamics method find the stability of these monolayers exhibiting unique electronic properties. For example, the BAs monolayer possesses a robust self-doping feature, whereas the BSb monolayer carries the intrinsic charge carrier concentration of the order of $10^{12}\,\mathrm{cm}^{-2}$ which is comparable to that of graphene. Moreover, the direction-dependent optical response is predicted in these B-based monolayers; a high IR response in the x-direction is accompanied with that in the visible region along the y-direction. The results are, therefore, expected to help in realizing the B-based devices for nanoscale applications.

Supplementary material for this article is available online

Keywords: DFT, anisotropic Dirac cone materials, boron-based monolayers, self-doping feature

(Some figures may appear in colour only in the online journal)

1. Introduction

Technological advancement has witnessed a huge upswing owing to the novel physics ushered by the discovery of graphene [1]. It has linear dispersion of bands around the Fermi level which causes the charge carriers to show ultrahigh mobility [2], quantum hall effect [3], and unique charge transport properties [4]. In the past decade, the potential of graphene for high-performance electronic and energy devices has led to the extensive exploration of other 2D Dirac materials beyond graphene, for instance, elemental 2D nanosheets of germanium and silicon [5], allotropes of carbon [6], and other Dirac cone materials such as Be_3C_2, AB_3 and A_3B (A, B = C, Si and Ge) binary monolayers, C_4N, FeB_2 and HfB_2 [7–11]. Besides the excellent carrier mobilities, graphene shows a considerable optical response from IR to UV region, making graphene a viable candidate for nano-photonics and electronics [12, 13]. However, the optical absorption of graphene is small in the low range of frequencies [14, 15] which poses a serious limitation for graphene-based optoelectronic devices.

The experimental synthesis of a 2D graphene-like analog of boron called borophene has given a big fillip to boron-based future nanodevices [16–20]. On account of the flexible and unique bonding nature of boron, it can also form many allotropes [19–21]. Besides being the lightest Dirac material,

---

* Authors to whom any correspondence should be addressed.

borophene exhibits a plethora of interesting properties [16, 22], phonon-mediated superconductivity [23], promising anode material for batteries [24, 25], a potential electrode material for nanoelectronics [26, 27], high mechanical strength [28] and good thermal conductivity [29, 30]. Over and above, borophene evinces strong anisotropy in both electronic and optical properties because of its typical electrical conductivity and high electron transparency along a non-wrinkled direction [31, 32]. This indicates that it can act as a transparent conductor [33].

Recent studies have also shown that boron has a good possibility of the formation of 2D compound monolayers that can yield new materials with excellent electronic and optical properties [11, 34–38]. The surface functionalization of borophene alters its electronic as well as optical properties to a significant extent leading to a notable optical conductivity observed in the visible region [32, 36]. The borophene hydrides [39] show an absorption edge in the visible range of light [35]. The recent experimental realizations of freestanding borophene (B_{12}, X_3, and intermediate phases) monolayers and that of reduced borophene oxide have been reported via sonochemical exfoliation, and are expected to expand the horizons of their applications [40]. Exploring the physics of 2D boron monolayers can complement the application of these monolayers in upcoming technologies.

Therefore, in this work, a novel phase of pristine borophene and boron-based hybrid monolayers BX (X = As, Sb, and Bi) have been studied systematically using density functional theory (DFT). Structural, electronic and optical properties have been explored for these monolayers. The optical responses based on the dielectric functions such as electron energy loss spectrum (EELS), absorption coefficient, refractive index and reflectivity are explored. In addition, the effect of spin-orbit interaction on the electronic and optical properties of these monolayers has also been examined.

2. Computational details

All the calculations are carried out within the framework of DFT as implemented in the Vienna *ab-initio* Simulation Package (VASP) [41]. The generalized gradient approximation, in Perdew, Burke, and Ernzerhof [42] parameterization has been used to describe the exchange-correlation effects. The electron-ion interactions are taken into account by using the projector augmented wave pseudopotential method [43]. The cutoff of plane-wave kinetic energy and the convergence criterion of energy for self-consistent calculations have been set to be 600 eV and 10^{-8} eV, respectively. A well converged set of $17 \times 11 \times 1$ k-point mesh has been employed for Brillouin zone integrations. The structural relaxations are performed to force tolerance of 10^{-8} eV Å^{-1} by computing the Hellmann–Feynman forces using the conjugate gradient algorithm. To ensure that the monolayers do not interact with their periodic images, a vacuum region of more than 10 Å along the z-axis is introduced. The studied monolayers are simulated in the rectangular 4-atoms unit cell. To explore the dynamic stability, phonon dispersion

spectra have been computed as implemented in the PHONOPY package [44] which employs the density functional perturbation theory and SCF data obtained using VASP. To test the thermal stability of the studied monolayers, we performed *ab-initio* molecular dynamics (AIMD) calculations for 5000 fs with a time step of 1 fs using a canonical ensemble. The Nose algorithm [45] is used to control the temperature in simulations. In the optical properties, the frequency-dependent imaginary part of the dielectric function is studied by the sum over empty band states method [46]. The imaginary part of the optical dielectric function is computed by using a well-converged mesh of $57 \times 51 \times 1$ k-points containing a total of 64 bands.

3. Results and discussion

The relaxed geometries of the studied monolayers have been presented in figures 1(a)–(d). The optimized lattice constants *a* (b) are 2.0 (5.93) Å, 3.39 (5.90) Å, 3.73 (6.48) Å, and 3.82 (6.75) Å, for pristine borophene, BAs, BSb, and BBi monolayers respectively. Note that the lattice constant of honeycomb borophene is 2.9 Å [47]. The lattice constants 3.39 and 3.73 Å for BAs and BSb are in agreement with earlier reported values for h-BAs and h-BSb [37]. It is to be noted that the geometries of the BX monolayers are not atomically flat, where X atoms are alternatively extended beyond the 2D plane as compared to the pristine borophene. There is an increase in buckling height in the aforementioned structures from 0.46 for BAs to 1.26 Å for BBi. The calculated bond lengths B–As, and B–Sb of hybrid monolayers are consistent with the previous studies [48, 49]. Calculated lattice parameters, bond lengths, bond angles, buckling heights and cohesive energies of relaxed structures are listed in table 1.

To understand the nature of chemical bonding in the considered monolayers, the electron localization function (ELF) plots [50] are shown in figures 1(e)–(h). Note that the range of ELF values varies from 0 to 1 and is related to electron density values. The ELF values 0.0, 0.5 and 1.0 indicate negligible small charge density, electron delocalization, and electron localization, respectively [10, 50]. The ELF map is sliced perpendicular to (001) direction for pristine and hybrid monolayers (figures 1(e)–(h)), where the red region with the large value of ELF is showing the localization of electrons at the center of the B–B bond which is the characteristic of covalent bonding. However, the electrons are localized around the X atoms for the B–X bonds.

3.1. Structural stability

To assess the energetic stability, the cohesive energies for hybrid BX (X = As, Sb and Bi) monolayers are calculated as follows:

$$E_{coh} = \{m(E_B) + n(E_X) - E_{BX}\} / \{m + n\}, \tag{1}$$

where E_B, E_X and E_{BX} are the total energies obtained for Boron, X (i.e. As, Sb, and Bi) atom and BX monolayer. *m* and
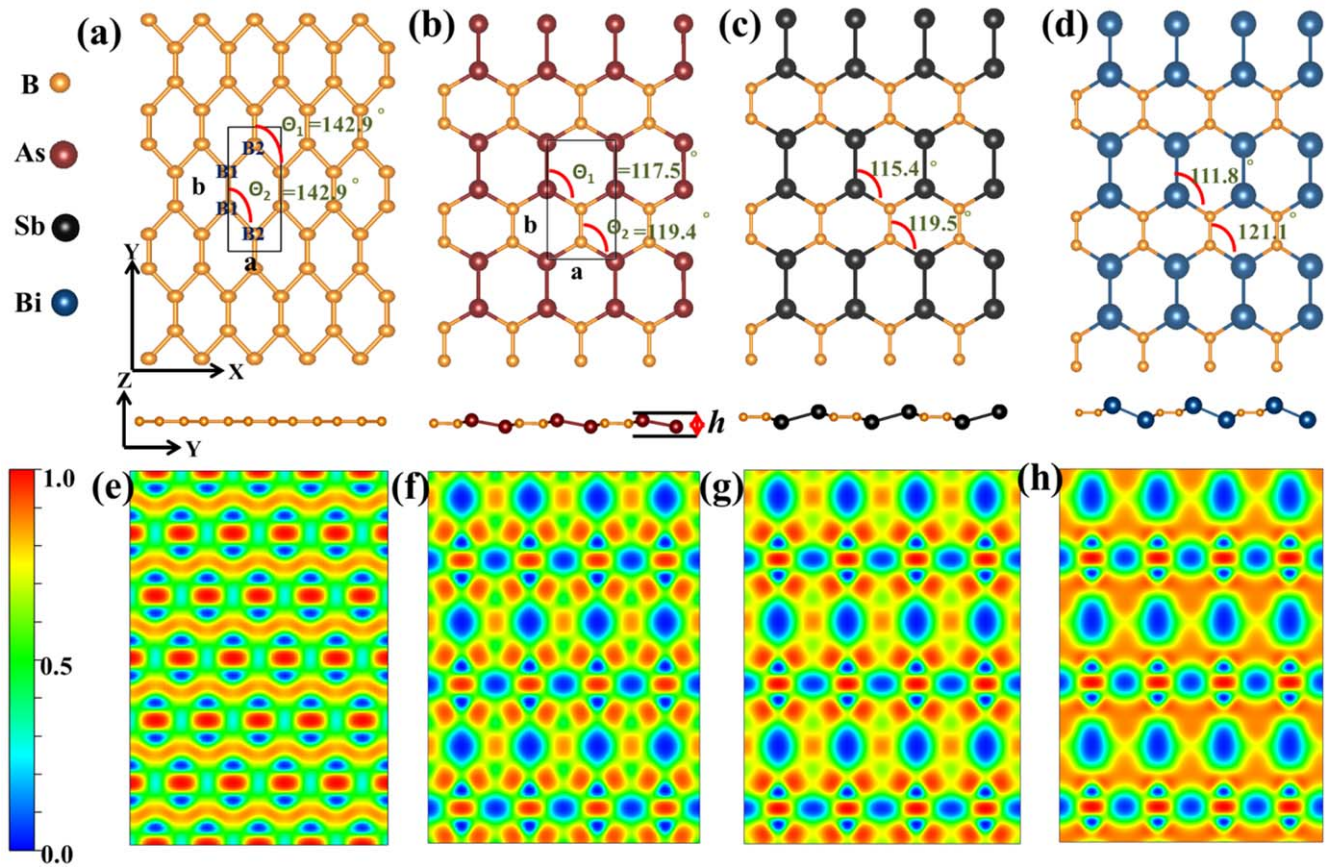
Figure 1. Geometrical structures with top and side views and ELF plots of pristine (a), (e), BAs (b), (f), BSb (c), (g), and BBi (d), (h) monolayers. h is the buckling height. Θ_1 and Θ_2 are the bond angles. Golden, brown, black, and blue balls denote the B, As, Sb and Bi atoms respectively.

Table 1. The calculated structural properties of pristine borophene (B1 and B2 are boron atoms) and boron-based hybrid BX (X = As, Sb and Bi) monolayers: lattice parameters a and b (Å), bond lengths (Å), bond angles Θ_1 and Θ_2 (°), buckling heights h (Å) and cohesive energy E_{coh} (eV/atom).

| Systems	a (Å)	b (Å)	Bond lengths (Å)			Bond Angles (°)		h (Å)	E_{coh} (eV/atom)
						Θ_1	Θ_2		
Pristine	2.00	5.93	B1–B1 = 1.63	B1–B2 = 1.66	—	142.9°	142.9°	0	2.67
BAs	3.39	5.90	B–B = 1.64	B–As = 1.97	As–As = 2.36	117.5°	119.4°	0.46	3.96
BSb	3.73	6.48	B–B = 1.63	B–Sb = 2.19	Sb–Sb = 2.78	115.4°	119.5°	0.74	3.54
BBi	3.82	6.75	B–B = 1.59	B–Bi = 2.33	Bi–Bi = 3.01	111.8°	121.1°	1.26	3.21

n are representing the total number of boron and X atoms respectively in BX hybrid monolayers.

We find that the cohesive energy decreases with the increase in the size of the X atom, which can be seen by the weakened bonding from B–As to B–Bi and the increase in lattice strain in the unit cell. However, the cohesive energies of hybrid monolayers are higher than that of the pristine monolayer. This indicates the higher energetic stability of the hybrid monolayers as compared to pristine borophene. Note that the calculated cohesive energies are less than that of borophosphene (4.82 eV/atom) [34], but larger than that of phosphorene (∼3.48 eV/atom [51, 52]).

The computed phonon dispersions for pristine and hybrid monolayers are shown in figures S1(a)–(d) (available online at stacks.iop.org/NANO/32/415203/mmedia) in the sup-plementary information (SI). The presence of soft imaginary modes of lattice vibrations for pristine borophene, BAs, BSb, and BBi monolayers in the vicinity of Γ-point in the Brillouin zone are indicating that the considered geometries are a result of a typical local minimum [11, 53]. However, the imaginary phonon modes decrease while going from pristine to BBi monolayer. It is inferred from the phonon spectra that the highest frequency of pristine borophene is 42.3 THz (figure S1(a) in SI) which is more than those of the hybrid mono-layers (figures S1(b)–(d) in SI). Further, for BAs, the highest frequency is 32 THz which is slightly larger than that of the borophosphene (∼28.5 THz) [34] showing that the B–As bond is robust in the BAs monolayer (figure S1(b) in SI).
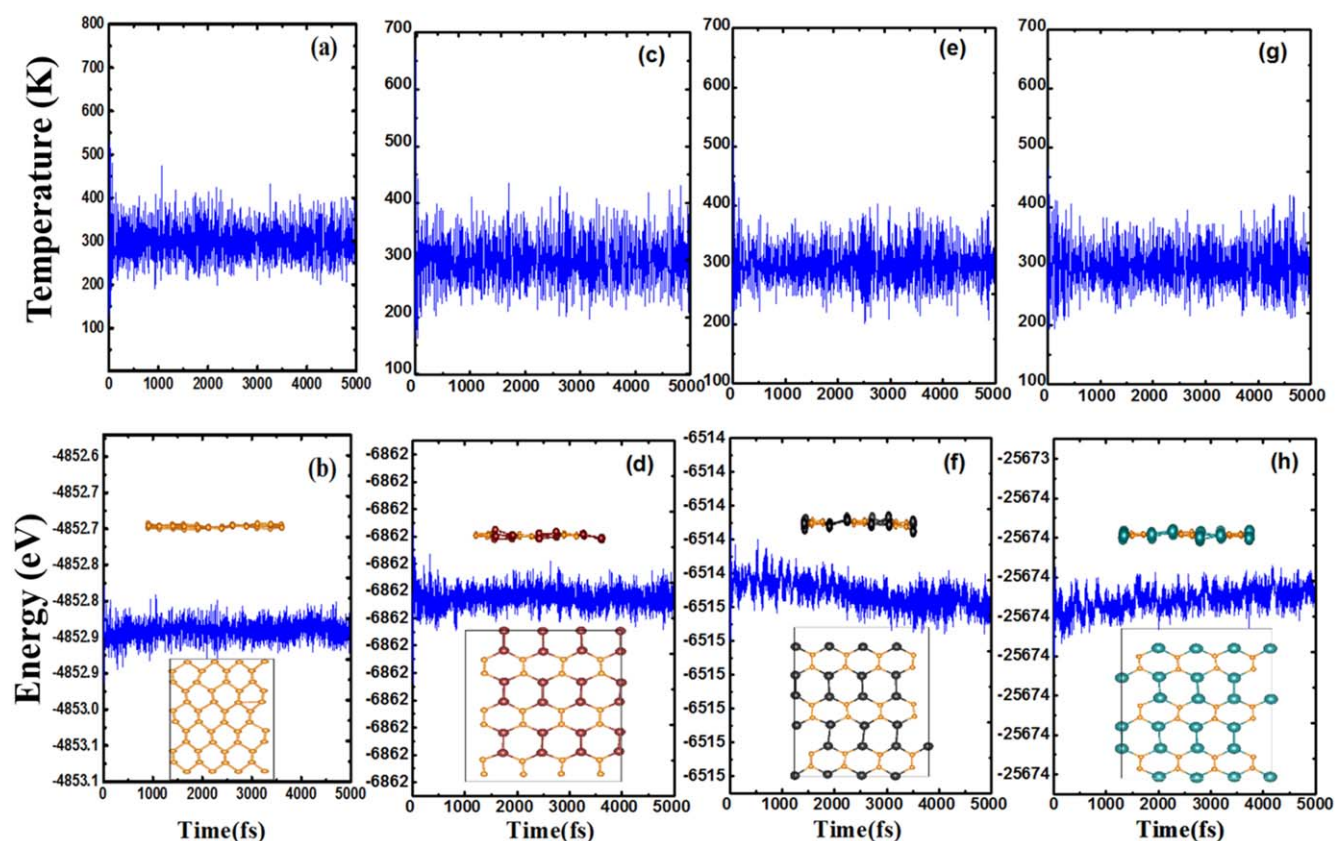
Figure 2. AIMD simulated curves w.r.t the temperature and energy of pristine (a), (b), BAs (c), (d), BSb (e), (f) and BBi (g), (h) monolayers respectively. Insets are displaying the side and top views of (b) pristine (d) BAs, (f) BSb, and (h) BBi monolayers at 5000 fs in the lower panel.

However, the highest frequency values obtained for BSb and BBi monolayers (31 and 30.5 THz) (figures S1(c) and (d) in SI) are slightly less than that of BAs monolayer. This can be attributed to the significantly larger atomic mass of pnictogen atoms (As, Sb and Bi) in comparison to pristine monolayer atoms.

Further, the thermal stability of the studied monolayers at room temperature is investigated by performing AIMD simulations (figure 2) using a 4×3 supercell. The curves of AIMD simulations for considered monolayers are showing the constant average energy (figures 2(a), (c), (e) and (g)) and temperature (figures 2(b), (d), (f) and (h)) over almost 5000 fs time steps. At the end of the simulations, final structures (top and side views) are obtained for the pristine borophene and BAs, BSb and BBi hybrid monolayers (insets of figures 2(b), (d), (f) and (h)) which preserve their structural integrity implying stability of these monolayers at room temperature.

3.2. Electronic properties

The calculated electronic band structures for the studied monolayers are depicted in figure 3. It is found that multiple bands cross the Fermi level at different locations in the Brillouin zone exhibiting the metallic nature of pristine borophene. Whereas the hybrid monolayers show the Dirac cones in their electronic band structures which exhibit a linear dispersion of valence and conduction bands close to the Fermi

level. In the electronic band structure calculated for BAs monolayer, the Dirac point (along $\Gamma-X$ direction) is slightly above (0.06 eV) the Fermi level (figure 3(b)) indicating that BAs is self-doped with holes. Whereas in the electronic band structure of BBi monolayer, there are two Dirac cones: one is slightly below (0.09 eV) and the second is slightly above (0.21 eV) the Fermi level (figure 3(d)) along with $\Gamma-X$ and $\Gamma-Y$ directions showing the self-doped nature of BBi monolayer. The first Dirac cone is nearer to the Fermi level than the second suggesting that electrons are present as charge carriers in the BBi monolayer. The self-doping characteristic is substantial to accomplish ultrahigh carrier mobility in Dirac cone materials because the Dirac point where the density of states is zero is slightly lower (higher) than the Fermi level exhibiting an n- (p-) type doping [54]. In borophosphene, this feature was developed by applying strain [34]. Similarly, in silicene and germanene, the strain-induced self-doping feature is observed which is related to the buckling height [55]. However, in the BX materials, the p-(n-) type intrinsic self-doping feature of carriers has been observed as the location of Dirac-point above (below) the Fermi level which can be associated with the buckled nature of monolayers [55, 56]. These hybrid monolayers can be used in high-speed analog electronics [57].

To understand the origin of Dirac states in hybrid monolayers, the contribution of different orbitals of atoms has been shown in orbital projected band structures (figures
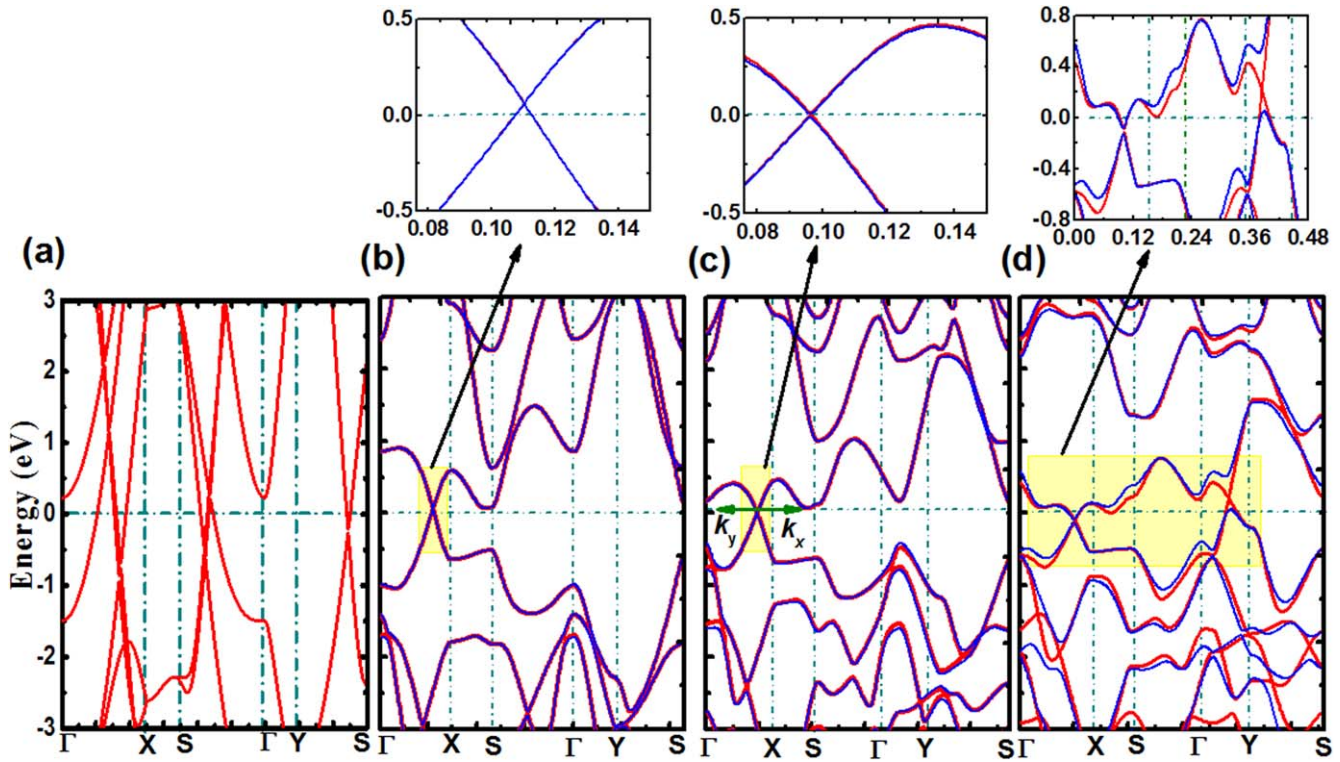
Figure 3. Electronic band structures for (a) pristine borophene without SOC (b) BAs (c) BSb and (d) BBi hybrid monolayers without (with) the inclusion of SOC represented by red (blue) color and with the highlighted part at the Fermi. The dashed line at 0 eV represents the Fermi level. The *X*-axis represents the values of *K* along with several high symmetry directions in the Brillouin zone.

S2(a)–(c). The main contribution to the CBM and VBM is found from p_z orbitals of B and As, Sb, and Bi for Dirac cone 1 of BAs, BSb, and BBi monolayers respectively. Whereas, the second Dirac cone has its contribution from p_z orbital of B and p_x orbital of Bi atom in BBi monolayer suggesting that the orbital hybridization plays a significant role in the formation of Dirac states.

Some of the X atoms in the studied BX hybrid monolayers have a large atomic number (like Bi) and hence the role of spin-orbit coupling (SOC) on the electronic properties of the materials becomes crucial. SOC is an interaction between the spin and orbital motion of the electron around the nucleus. This coupling causes a shift in the atomic energy levels of electrons due to the electromagnetic interaction between the spin of the electron and the electric field of the nucleus. In calculations, the SOC effect is incorporated by the diagonalization of the total Hamiltonian which contains the spin-orbit interaction and the self-consistently determined Kohn–Sham Hamiltonian [58]. The impact of SOC on the electronic properties is presented in figures 3(b)–(d). It can be observed that the incorporation of SOC has no significant effect on the electronic properties of BAs and BSb (figures 3(b), (c)) monolayers. However, a significant SOC-induced splitting of bands is observed in the BBi monolayer which can be due to the relativistic effects resulting from a heavy atom (Bi) core. Splitting is more prominent for the states slightly above the Fermi level along Γ−Y direction, as compared to those along Γ−X direction below the Fermi level (figure 3(d)). Interestingly, the observed Dirac point above Fermi level disappears

with the inclusion of SOC in BBi monolayer. A significant SOC-induced splitting of bands is observed which is due to the relativistic effects resulting from a heavy atom core. Moreover, gaps of 30 meV and 460 meV are opened up for Dirac points (1 and 2) along Γ−X and Γ−Y respectively.

3.2.1. Fermi velocity and carrier concentration. Dirac cones observed in the band structures of BAs, BSb, and BBi possess different slopes (and hence different Fermi velocities) along K_x and K_y directions (directions are shown in figure 3(c)) implying an anisotropic character of the Dirac cone in these systems. Note that Fermi velocity is calculated from the slope obtained by linearly fitting the bands near Dirac point as below:

$$V_f = \frac{1}{\hbar} \frac{\partial E}{\partial k} \qquad (2)$$

The calculated Fermi velocities for BAs, BSb, and BBi hybrid monolayer are 5.87, 4.59, and 3.39($\times 10^5$ m s^{-1}) along K_x direction and 5.11, 4.42 and 3.11 ($\times 10^5$ m s^{-1}) along K_y direction. Different Fermi velocities along the different directions confirm anisotropy in Dirac cones and hence in transport properties. The magnitudes of Fermi velocities obtained in BAs, BSb, and BBi monolayers are comparable to the values reported for borophosphene (6.51(4.71) $\times$ 10^5 m s^{-1} along K_x (K_y) direction) [34]. Note that the order of magnitude of Fermi velocities of the studied hybrid monolayers is also comparable to that of graphene (8.2 $\times$ 10^5 m s^{-1}) [54].

Table 2. The calculated values for Fermi velocity (V_f), Fermi level, and Dirac point difference ΔE_d and doping charge carrier concentration ($N_{h/e}$) for BAs and BBi hybrid monolayers.

Systems	V_f ($\times 10^5$ ms^{-1})	ΔE_d (meV)	$N_{h/e}$ ($\times 10^{12}$ cm^{-2})
BAs	5.11–5.87	60	$N_h = 1.01$–0.77
BBi	3.11–3.39	−90	$N_e = 6.16$–5.18

The intrinsic charge carrier concentration of a material can give an idea about the materials for future generations' devices. Unlike conventional semiconductors (silicon and germanium), the level of intrinsic carriers in graphene is an order of magnitude less sensitive to the temperature. Due to this, the electronic properties of a properly fabricated graphene-based transistor or p–n junction will sustain before other parts melt at high temperatures (above 1500 K) [59]. The intrinsic charge carrier concentration of a material [60] can be obtained as:

$$n = \frac{\pi k_B{}^2 T^2}{6\hbar^2 V_f{}^2} \quad (3)$$

where k_B is Boltzmann constant, V_f is Fermi velocity, $T = 300$ K, and $\hbar$ is reduced Planck constant. The calculated intrinsic charge carrier concentration for the BSb monolayer varies from 0.41 to 0.38 $\times$ 10^{12} cm^{-2} which is larger than that of graphene (6×10^{10} cm^{-2} [61]) and may be attributed to the anisotropic Fermi velocities.

The charge carrier concentrations of p-(n-) type doping of BAs (BBi) monolayer where the Fermi levels are little shifted as compared to the BSb monolayer can be calculated by using [59, 62]:

$$N_{h/e} = \frac{(\Delta E_d)^2}{\pi (\hbar V_f)^2} \quad (4)$$

here ΔE_d represents the difference between the Fermi level and Dirac point of the monolayers. Calculated values for hole (electron) charge carrier concentrations for BAs (BBi) vary from 1.01 to 0.77 $\times$ 10^{12} cm^{-2} (from 6.16 to 5.18 $\times$ 10^{12} cm^{-2}) due to different Fermi velocities (table 2).

The Fermi velocities for BBi monolayer after the inclusion of SOC effect are calculated to be 2.8 (2.3) $\times$ 10^5 m s^{-1} along $K_x(K_y)$ directions, thus, the electron charge carrier concentrations are obtained to be 7.59 (11.26) $\times$ 10^{12} cm^{-2}. The higher carrier concentrations with SOC are due to lower Fermi velocities as compared to those without SOC (table 2). The feature worth highlighting is that BAs and BSb monolayers have rather robust Dirac points and preserve their features even after incorporating SOC.

3.3. Optical properties

The optical properties of the studied monolayers can be obtained from the complex dielectric function. The complex dielectric function is defined as $\epsilon(\omega) = \epsilon_1(\omega) + i\epsilon_2(\omega)$ with $\epsilon_1(\omega)$ and $\epsilon_2(\omega)$ being real and imaginary parts of the dielectric function. Within independent particle approximation, the imaginary part of the dielectric function can be determined

by taking the sum over the empty band states using the equation [46].

$$\epsilon_{2,\,\alpha\beta}(\omega) = \frac{4\pi^2 e^2}{\Omega} \lim_{q \to 0} \frac{1}{q^2} \sum_{k,c,v}^{\infty} 2\omega_k \delta(\epsilon_{ck} - \epsilon_{vk} - \omega)$$
$$\times \langle u_{ck+e_\alpha q} | u_{vk} \rangle \langle u_{ck+e_\beta q} | u_{vk} \rangle^*. \quad (5)$$

Here, ω is the frequency, Ω is the volume of the unit cell, v and c refer to the valence and conduction band states, k is the wave vector and $u_{c,k}$ ($u_{v,k}$) represents the wave function of the conduction (valence) band states at the k points. Here, α and β correspond to Cartesian components and e_α and e_β are unit vectors for three x, y, and z directions. '*' represents the complex conjugate of a wavefunction. Within DFT, the wave function of the electrons can be obtained by employing Kohn–Sham orbitals. The real part of the dielectric function $\epsilon_1(\omega)$ can be obtained from imaginary parts by employing Kronig–Kramers relations [46, 63]. Once we have the dielectric function, other optical properties like EELS, absorption coefficients $\alpha(\omega)$, refractive index $n(\omega)$ and reflectivity $R(\omega)$ of the monolayers can be calculated as described in [14, 31, 64] and equations are given in SI.

The optical properties of the pristine borophene and hybrid monolayers are calculated with the polarization of the electromagnetic field in x and y directions. The structure peaks in the imaginary part of the dielectric function may be attributed to the multiple inter-band transitions among the energy bands appearing along with various directions in the Brillouin zone. Therefore, one has to consider a volume integral in the whole Brillouin zone to account for all interband transitions corresponding to a particular energy.

Figure 4(a) represents the imaginary part of studied monolayers for x- and y-polarizations. The peaks in $\epsilon_2(\omega)$ for pristine borophene are found in UV (Visible) region of light at energies 7.84 eV (1.78 eV) in x-(y-) polarization. The prominent structure peak is B located at 1.78 eV for y-polarization as compared to peak A at 7.84 eV for x-polarization (figure 4(a)) for pristine borophene. The sharp peaks at the particular energy are probably due to the presence of approximately parallel bands above and below Fermi level and the inter-band transitions are occurring from occupied states below Fermi level at the same energy [65]. The optical inter-band transitions occurring from valence bands below the Fermi level to the conduction bands above the Fermi level in the electronic band structure of pristine borophene are designated as A and B (figure S3(a) in SI). The hybrid BX (X = As, Sb and Bi) monolayers show strong peaks in x-polarization at 0.75, 0.82 and 0.61 eV (IR region) as compared to at 6.05, 4.92 and 4.36 eV (UV region) where approximately parallel bands are found (figure 4(a) and (figures S3(b)–(d) in SI)). In y-polarization, the peaks start rising from very close to 0 eV. At energies 1.94, 4.41 and 5.21 eV (BAs), 1.86 and 3.61 eV (BSb) and 2.02 and 3.00 eV (BBi) the optical interband transitions are possible in visible and UV regions (figure 4(a)).

The optical interband transitions are evident from the electronic band structures of BAs, BSb, and BBi monolayers (figures S3(b)–(d) in SI). Interband transitions (designated as
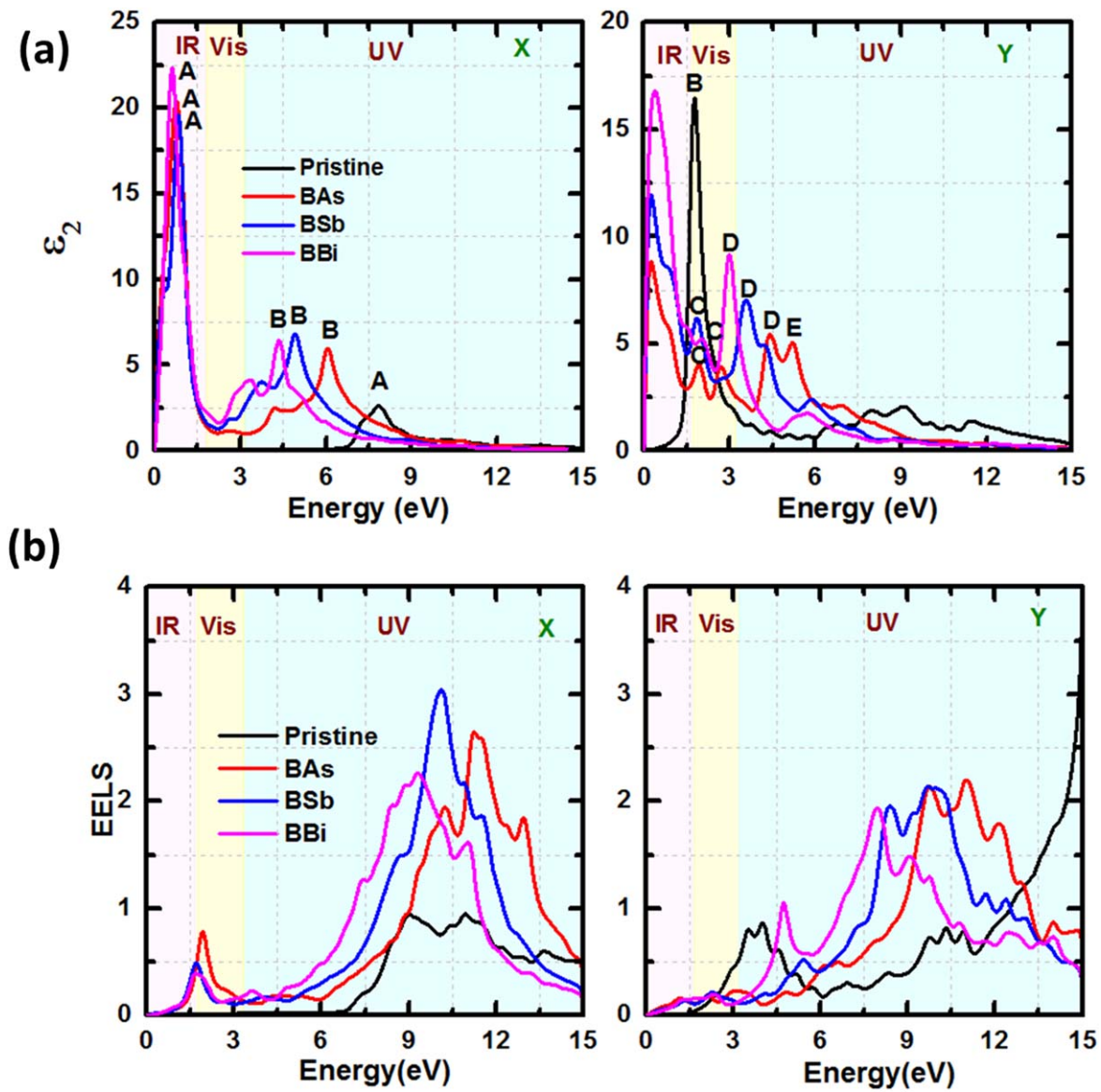
Figure 4. (a) Imaginary part of the dielectric function and (b) electron energy loss function of pristine and hybrid monolayers BX (X = As, Sb and Bi) for *x* (left panel) and *y* (right panel) polarizations.

Table 3. The optical properties of pristine and hybrid monolayers BX (X = As, Sb and Bi). The positions of major peaks in the imaginary part (ϵ_2) of the dielectric function and plasmons energy (eV) for both *x* and *y* polarizations.

Systems	Peak positions in ϵ_2		Plasmon energy (eV)	
	Polarizations			
	x	*y*	*x*	*y*
Pristine	7.84 (A)	1.78 (B)	8.98, 10.94	4.03, 10.32
BAs	0.75, 6.05 (A, B)	1.94, 4.41, 5.21 (C, D, E)	1.91, 10.28, 11.23	9.74, 11.01, 12.14
BSb	0.82, 4.92 (A, B)	1.86, 3.61 (C, D)	1.69, 10.12	8.40, 9.72, 11.68
BBi	0.61, 4.36 (A, B)	2.02, 3.00 (C, D)	1.68, 9.28	4.74, 7.96, 9.00

A, B, C, D, and E) in BX monolayers are excited from occupied valence bands and shallow core levels to the unoccupied conduction bands. It is observed that the interband transitions get red-shifted from pristine to BX monolayers in both *x* and *y* polarizations (table 3). Among hybrid

monolayers, the peaks B and D get red-shifted as the size of the X atom increases from BAs to BBi monolayers. The energies of the optical interband transitions of studied monolayers in both polarizations are comparable to those of borophene [31]. The peak positions in both orientations are

Table 4. The optical parameters of pristine and hybrid monolayers BX (X = As, Sb and Bi): static refractive indexes, maximum refractive index (Energy (eV)), and maximum reflectivity percentage (Energy (eV)) for both x and y polarizations.

Systems	Pristine		BAs		BSb		BBi	
Polarizations	x	y	x	y	x	y	x	y
Static refractive index	1.24	2.5	5.1	4.5	4.85	5.2	4.97	5.9
Maximum refractive index (Energy (eV))	1.82 (7.04)	4.02 (1.61)	2.09 (5.9)	2.31 (4.20)	2.15 (4.75)	2.4 (3.35)	2.10 (4.17)	2.53 (2.83)
Maximum reflectivity (%) (Energy (eV))	16 (8.1)	49 (1.94)	58 (1.19)	34 (5.45)	54 (1.04)	39 (4.55)	51 (0.65)	47 (3.44)

different and this can be attributed to the anisotropic nature of these monolayers.

Based on the real part of the dielectric function, the electronic polarizability of studied monolayers can be analyzed. The static dielectric constants are calculated for pristine borophene, BAs, BSb, and BBi at the zero-energy value for both the polarizations (x and y) (figure S4 in SI). In x-polarization, the values are 1.5, 26.20, 23.76, and 24.73, whereas in y-polarization the static dielectric constants are 6.26, 20.18, 26.98, and 34.28 for pristine, BAs, BSb, and BBi monolayers respectively. These values suggest that the BBi monolayer has the relatively highest polarizability in y-polarization. Moreover, an anisotropic character of electronic polarization is also reflected in the above data.

The calculated EELS in both x and y polarizations is shown in figure 4(b) which describes the loss of energy of the electron when it oscillates rapidly in the material. The peaks that appear in the EELS represent the plasmon resonance resulting from the collective excitations of the free electrons. The values are listed in table 3 for x and y polarizations. The electron energy loss function of pristine borophene shows broad resonance peaks at about 8.98 and 10.94 eV for x polarization and 4.03 and 10.32 eV for y polarization (peaks correspond to the values 4.55 and 11.47 eV of borophene in y-polarization [31]) all of which lie in the UV region. These peaks are corresponding to the energies of collective excitations in the electronic charge density and suggest the optical response in the UV region for pristine borophene. On the other hand, BAs, BSb, and BBi monolayers show Plasmon peaks in the visible and UV region for x-polarization and in the UV region for y polarization. For x-polarization, the resonance peaks are found at energies 1.91, 10.28, 11.23 eV (BAs), 1.69, 10.12 eV (BSb) and 1.68, 9.28 eV (BBi). For y-polarization, the major peaks are found at energies 9.74, 11.01, 12.14 eV (BAs), 8.40, 9.72, 11.68 eV (BSb) and 4.74, 7.96, 9.00 eV (BBi). A redshift is observed in many peaks with an increase in atomic size going from BAs to BBi monolayers. From EELS analysis, it is found that BX monolayers may exhibit good optical responses in IR, the lower part of the UV region for both x- and y-polarizations. EELS exhibit additional peaks in the visible region as well for y-polarization. New peaks in EELS spectra of hybrid monolayers as compared to the pristine case may have originated from the buckling effect of monolayers [66]. On analyzing the EELS, it is observed that the energy trends of peaks in both orientations are not regular due to the anisotropic nature of these monolayers. Also, the electronic behavior of these monolayers is different from each other which plays a large role in determining the optical properties.

In absorption spectra for studied monolayers, the absorption coefficients (α) (figure S5 in SI) show a large order of magnitude 10^4 cm^{-1} for both x and y polarizations. The pristine borophene shows absorption in the UV (visible and UV) region of light at 8.02 eV (1.96 and 9.35 eV) for x- (y-) polarizations. In the case of BAs, BSb, and BBi monolayers, the absorption coefficients start increasing from 0 eV suggesting the semi-metallic or metallic nature of these monolayers. The peaks of absorption in hybrid monolayers are found at the energy values 1.11, 6.23 (2.01, 5.41) eV for BAs, 1.05, 5.14 (1.97, 4.44) eV for BSb and 1.22, 4.53 (2.19, 3.21) eV for BBi monolayer respectively in x-(y-) polarization. Also, a redshift in peak energies can be inferred from the above data while going from pristine borophene to BX monolayers in both x and y polarizations.

The optical constant, refractive index of studied monolayers has been calculated and depicted in figure S6 in SI. The refractive index spectra reveal that the static refractive index of BAs monolayer (5.1) is higher than those of pristine borophene (1.24), BSb (4.85), and BBi (4.97) in x-polarization. In y-polarization, BBi monolayer has a larger static refractive index (5.9) than those of pristine borophene (2.5), BAs (4.5) and BSb (5.2). The maximum refractive index for pristine borophene is 1.82 (4.02) at 7.04 (1.61) eV in x-(y-) polarization. In case of hybrid monolayers, the maximum refractive indices are observed for BAs (2.09), BSb (2.15) and BBi (2.10) monolayers at 5.9, 4.75 and 4.17 eV in x-polarization. In y-polarization BAs (BSb) monolayer has shown maximum refractive index 2.31 (2.4) at 4.20 (3.35) eV and BBi monolayer has shown maximum refractive index 2.53 at 2.83 eV in y-polarization. The refractive indices show an increase as one goes from pristine to BX monolayers. The values of the optical constant are summarized in table 4.

Further, multiple peaks are located in the energy range of 0–10 eV of the reflectivity spectra of pristine and BX monolayers in both polarizations (x and y) (figure S7 in SI). The maximum reflection is found to be 58% at 1.19 eV for BAs which is larger than those of BSb (54% at 1.04 eV), BBi (51% at 0.65 eV) in low energy region (IR) and for pristine borophene 16% at 8.1 eV in x-polarization. In y-polarization, the maximum reflection is found for pristine borophene (49%) in the visible region as compared to BAs (34%), BSb (39%), and BBi (47%) monolayers in the UV region of light. The

values of optical constants are summarized in table 4. Based on anisotropic dielectric properties the aforementioned monolayers can be used in a variety of applications for optoelectronic devices.

Further, the optical responses studied with SOC are showing slightly varied positions of peaks from those without SOC for both x and y polarizations. Moreover, the peak values of the two polarizations are not the same and exhibit strong anisotropic characteristics of the BBi monolayer with (without) SOC (refer to figure S8 and relevant text in SI for more details).

4. Conclusions

In summary, DFT based study of anisotropic 2D borophene and B-based hybrid BX (X = As, Sb and Bi) monolayers has been conducted. Calculated cohesive energy, phonon spectra, and AIMD simulations indicate that the studied monolayers are structurally and thermodynamically stable and have a good possibility of their experimental synthesis. The anisotropy in Dirac cones results in varied carrier concentrations resulting from anisotropic Fermi velocity in BX monolayers. The p-type and n-type self-doping characteristics are observed for BAs and BBi monolayers without SOC. With SOC p-type self-doping character of BAs is robust. Unlike borophosphene, the self-doping feature in BAs does not require any additional atom adsorptions or external strains making BAs monolayer unique. On the other hand, SOC has introduced gaps of 30 and 460 meV in Dirac points shown below and above the Fermi level in BBi monolayer. In optical properties, the interband transitions get red-shifted from pristine to hybrid monolayers in x-polarization and blue-shifted in y-polarization. Also, the loss function gets red-shifted from BAs to BBi monolayer with the increase in the size of atoms from As to Bi. Consequently, the optical response is optimized in hybrid monolayers in both the polarizations as compared to pristine borophene. High optical absorption is found in the IR region in x-polarization and low region of UV in both x and y polarizations along with the visible region in y-polarization. These characteristics of studied monolayers make them promising candidates for future optoelectronic devices such as IR spectroscopy, night vision devices, IR thermometers, thermographic cameras, and UV–visible spectroscopy.

Acknowledgments

Data availability statement

The data that support the findings of this study are available upon reasonable request from the authors.

ORCID iDs

Neha Katoch ⓘ https://orcid.org/0000-0001-9140-6433
Ashok Kumar ⓘ https://orcid.org/0000-0003-3636-0502
Jagdish Kumar ⓘ https://orcid.org/0000-0003-2115-3180
Ravindra Pandey ⓘ https://orcid.org/0000-0002-2126-1985

References

[1] Geim A K and Novoselov K S 2007 The rise of graphene *Nat. Mater.* **6** 183–91
[2] Bolotin K I, Sikes K J, Jiang Z, Klima M, Fudenberg G, Hone J, Kim P and Stormer H L 2008 Ultrahigh electron mobility in suspended graphene *Solid State Commun.* **146** 351–5
[3] Jiang Z, Zhang Y, Tan Y, Stormer H L and Kim P 2007 Quantum Hall effect in graphene *Solid State Commun.* **143** 14–9
[4] Bliokh Y P, Freilikher V and Nori F 2013 Ballistic charge transport in graphene and light propagation in periodic dielectric structures with metamaterials: a comparative study *Phys. Rev.* B **245134** 1–14
[5] Cahangirov S, Topsakal M, Aktu E and Ciraci S 2009 Two- and one-dimensional honeycomb structures of silicon and germanium *Phys. Rev. Lett.* **236804** 1–4
[6] Xu L C, Wang R Z, Miao M S, Wei X L, Chen Y P, Yan H, Lau W M, Liu L M and Ma Y M 2014 Two dimensional dirac carbon allotropes from graphene *Nanoscale* **6** 1113–8
[7] Wang B, Yuan S, Li Y, Shi L and Wang J 2017 A new dirac cone material: a graphene-like Be_3C_2 monolayer *Nanoscale* **9** 5577
[8] Qin X, Wu Y, Liu Y, Chi B, Li X, Wang Y and Zhao X 2017 Origins of Dirac cone formation in AB_3 and A_3B (A, B = C , Si , and Ge) binary monolayers *Sci. Rep.* **7** 10546
[9] Pu C, Zhou D, Li Y, Liu H, Chen Z, Wang Y and Ma Y 2017 Two-dimensional C_4N global minima: unique structural topologies and nano-electronic properties *J. Phys. Chem.* C **121** 2669
[10] Zhang H, Li Y, Hou J, Du A and Chen Z 2016 Dirac state in the FeB_2 monolayer with graphene-like boron sheet *Nano Lett.* **16** 6124–9
[11] Liu Z, Wang P, Cui Q, Yang G and Jin S 2019 Theoretical prediction of HfB_2 monolayer, a two- dimensional dirac cone material with remarkable Fermi velocity *RSC Adv.* **9** 2740–5
[12] Fai Mak K, Ju L, Wang F and Heinz T F 2012 Optical spectroscopy of graphene: from the far infrared to the ultraviolet *Solid State Commun.* **152** 1341–9
[13] Xia F, Mueller T, Lin Y, Valdes-garcia A and Avouris P 2009 Ultrafast graphene photodetector *Nat. Nanotechnol.* **4** 839–43
[14] Kumar A, Sachdeva G, Pandey R and Karna P S 2020 Optical absorbance in multilayer two- dimensional materials: graphene and antimonene optical absorbance in multilayer two-dimensional materials: graphene and antimonene *Appl. Phys. Lett.* **116** 263102

[15] Miller O D, Ilic O, Christensen T, Reid M T H, Atwater H A, Joannopoulos J D, Soljac M and Johnson S G 2017 Limits to the optical response of graphene and two-dimensional materials *Nano Lett.* **17** 5408–15

[16] Mannix A J *et al* 2015 Synthesis of borophenes: anisotropic, two-dimensional boron polymorphs *Science* **350** 1513–6

[17] Feng B, Zhang J, Zhong Q, Li W, Li S, Li H, Cheng P, Meng S, Chen L and Wu K 2016 Experimental realization of two-dimensional boron sheets *Nat. Chem.* **8** 563–8

[18] Kong X, Liu Q, Zhang C, Peng Z and Chen Q 2017 Elemental two-dimensional nanosheets beyond graphene *Chem. Soc. Rev.* **46** 2127–57

[19] Zhang Z, Penev E S and Yakobson B I 2017 Two-dimensional boron: structures, properties and applications *Chem. Soc. Rev.* **46** 6746–63

[20] Mannix A J, Zhang Z, Guisinger N P, Yakobson B I and Hersam M C 2018 Borophene as a prototype for synthetic 2D materials development *Nat. Nanotechnol.* **13** 444–50

[21] Lau K C and Pandey R 2008 Thermodynamic stability of novel boron sheet configurations *J. Phys. Chem.* B **112** 10217–20

[22] Feng B *et al* 2017 Dirac fermions in borophene *Phys. Rev. Lett.* **118** 096401

[23] Gao M, Li Q, Yan X and Wang J 2017 Prediction of phonon-mediated superconductivity in borophene *Phys. Rev.* B **95** 024505

[24] Liang P, Cao Y, Tai B, Zhang L, Shu H, Li F, Chao D and Du X 2017 Is borophene a suitable anode material for sodium ion battery? *J. Alloys Compd.* **704** 152–9

[25] Chen H, Zhang W, Tang X, Ding Y, Yin J, Jiang Y, Zhang P and Jin H 2018 First principles study of P-doped borophene as anode materials for lithium ion batteries *Appl. Surf. Sci.* **427** 198–205

[26] Yang J, Quhe R, Feng S, Zhang Q, Lei M and Lu J 2017 Interfacial properties of borophene contacts with two-dimensional semiconductors *Phys. Chem. Chem. Phys.* **19** 23982–9

[27] Katoch N, Kumar A, Sharma R, Ahluwalia P K and Kumar J 2020 Strain tunable Schottky barriers and tunneling characteristics of borophene/MX₂ van der Waals heterostructures *Physica* E **120** 113842

[28] Zhang Z, Yang Y, Penev E S and Yakobson B I 2017 Elasticity, flexibility, and ideal strength of borophenes *Adv. Funct. Mater.* **27** 1605059

[29] Sun H and Wan X G 2016 First-principles study of thermal properties of borophene *Phys. Chem. Chem. Phys.* **18** 14927–32

[30] Hu Y, Yin Y, Li S, Zhou H, Li D and Zhang G 2020 Three-fold enhancement of in-plane thermal conductivity of borophene through metallic atom intercalation *Nano Lett.* **20** 7619–26

[31] Peng B, Zhang H, Shao H and Xu Y 2016 The electronic, optical, and thermodynamic properties of borophene from first-principles calculations *J. Mater. Chem.* C **4** 3592–8

[32] Mogulkoc A, Mogulkoc Y, Kecik D and Durgun E 2018 The effect of strain and functionalization on the optical properties of borophene *Phys. Chem. Chem. Phys.* **20** 21043–50

[33] Adamska L, Sadasivam S, Foley J J, Darancet P and Sharifzadeh S 2018 First-principles investigation of borophene as a monolayer transparent conductor *J. Phys. Chem.* C **122** 4037–45

[34] Zhang Y *et al* 2019 Borophosphene: a new anisotropic dirac cone monolayer with a high fermi velocity and a unique self-doping feature *J. Phys. Chem. Lett.* **10** 6656–63

[35] Mortazavi B, Makaremi M, Shahrokhi M and Raeisi M 2018 Borophene hydride: a stiff 2D material with high thermal conductivity and attractive optical and electronic properties *Nanoscale* **10** 3759–68

[36] Grazianetti C, Cinquanta E, Molle A, Lherbier A, Botello-méndez A R and Charlier J 2016 Electronic and optical properties of pristine and oxidized borophene *2D Mater.* **3** 045006

[37] Shu H, Guo J and Niu X 2019 Electronic, photocatalytic and optical properties of two-dimensional boron pnictides *J. Mater. Sci.* **54** 2278–88

[38] Zhao Y, Li X, Liu J, Zhang C and Wang Q 2018 A new anisotropic dirac cone material: a B2S honeycomb monolayer *J. Phys. Chem. Lett.* **9** 1815–20

[39] Nishino H *et al* 2017 Formation and characterization of hydrogen boride sheets derived from MgB2 by cation exchange *J. Am. Chem. Soc.* **139** 13761–9

[40] Ranjan P, Sahu T K, Bhushan R, Yamijala S SRKC, Late D J, Kumar P and Vinu A 2019 Freestanding borophene and its hybrids *Communication* **31** 1900353

[41] Kresse G and Furthmüller J 1996 Efficient iterative schemes for *ab initio* total-energy calculations using a plane-wave basis set *Phys. Rev.* B **54** 11169–86

[42] Perdew J P, Chevary J A, Vosko S H, Jackson K A, Pederson M R, Singh D J and Fiolhais C 1993 Erratum: atoms, molecules, solids, and surfaces: applications of the generalized gradient approximation for exchange and correlation *Phys. Rev.* B **48** 4978

[43] Blöchl P E 1994 Projector augmented-wave method *Phys. Rev.* B **50** 17953–79

[44] Togo A and Tanaka I 2015 First principles phonon calculations in materials science *Scr. Mater.* **108** 1–5

[45] Nose S 1984 A unified formulation of the constant temperature molecular dynamics methods *J. Chem. Phys.* **81** 511

[46] Gajdoš M, Hummer K, Kresse G, Furthmüller J and Bechstedt F 2006 Linear optical properties in the projector-augmented wave methodology *Phys. Rev.* B **73** 045112

[47] Li W, Kong L, Chen C, Gou J, Sheng S, Zhang W, Li H, Chen L, Cheng P and Wu K 2018 Experimental realization of honeycomb borophene *Sci. Bull.* **63** 282–6

[48] Peng B, Zhang H, Shao H, Ning Z, Xu Y, Ni G, Lu H, Zhang D W and Zhu H 2017 Stability and strength of atomically thin borophene from first principles calculations *Mater. Res. Lett.* **5** 399–407

[49] Zhou Z Z, Liu H J, Fan D D and Cao G H 2019 A comparative study of the thermoelectric performance of graphene-like BX (X = P , As , Sb) monolayers *J. Phys. Condens. Matter* **31** 385701

[50] Becke A D and Edgecombe K E 1990 A simple measure of electron localization in atomic and molecular systems A simple measure of electron localization in atomic and molecular systems *J. Chem. Phys.* **92** 5397–403

[51] Hu W and Yang J 2015 Defects in phosphorene *J. Phys. Chem.* C **119** 20474–80

[52] Wang C, You Y and Choi J H 2020 First-principles study of defects in blue phosphorene *Mater. Res. Express* **7** 015005

[53] Şahin H, Cahangirov S, Topsakal M, Bekaroglu E, Akturk E, Senger R T and Ciraci S 2009 Monolayer honeycomb structures of group-IV elements and III-V binary compounds: first-principles calculations *Phys. Rev.* B **80** 155453

[54] Malko D, Neiss C, Vin F and Görling A 2012 Competition for graphene: graphynes with direction-dependent dirac cones *Phys. Rev. Lett.* **108** 086804

[55] Wang Y and Ding Y 2013 Strain-induced self-doping in silicene and germanene from first-principles *Solid State Commun.* **155** 6–11

[56] Zhang C, Jiao Y, Ma F, Bottle S, Zhao M, Zhongfang C and Aijun D 2017 Predicting a graphene-like WB4 nanosheet with double dirac cone, the ultra-high fermi velocity and significant gap opening by spin–orbit coupling *Phys. Chem. Chem. Phys.* **19** 5449–53

[57] Avouris P and Dimitrakopoulos C 2012 Graphene: synthesis and graphene, since the demonstration of its easy isolation by the exfoliation of *Mater. Today* **15** 86–97

[58] Steiner S, Khmelevskyi S, Marsmann M and Kresse G 2016 Calculation of the magnetic anisotropy with projected-augmented-wave methodology and the case study of disordered $Fe_{1-x}Co_x$ alloys *Phys. Rev.* B **93** 224425

[59] Yin Y, Cheng Z, Wang Li, Jin K and Wang W 2014 Graphene, a material for high temperature devices—intrinsic carrier density, carrier drift velocity, and lattice energy *Sci. Rep.* **4** 5758

[60] Fang T, Konar A, Xing H and Jena D 2007 Carrier statistics and quantum capacitance of graphene sheets and ribbons *Appl. Phys. Lett.* **91** 092109

[61] Ristein J, Mammadov S and Seyller Th 2012 Origin of doping in quasi-free-standing graphene on silicon carbide *Phys. Rev. Lett.* **108** 246104

[62] Hu W, Li Z and Yang J 2013 Electronic and optical properties of graphene and graphitic ZnO nanocomposite structures *J. Chem. Phys.* **138** 124706

[63] Lucarini V, Saarinen J J, Peiponen K-E and Vartiainen E M 2005 *Kramers–Kronig Relations in Optical Materials Research* (Germany: Springer-Verlag Berlin Heidelberg)

[64] Wooten F 1972 *Optical Properties of Solids* (New York: Academic)

[65] Fox M 2001 *Optical Properties of Solids* (New York: Oxford University Press)

[66] Das R, Chowdhury S, Majumdar A and Jana D 2015 Optical properties of P and Al doped silicene: a first principles study *RSC Adv.* **5** 41–50